Time-resolved internal-electron-scattering effect of H_2^+ in enhanced ionization regions

Yang Li,[1] Yueming Zhou,[1,*] Mingrui He,[1] Min Li,[1] Pengfei Lan,[1] and Peixiang Lu[1,2,†]

[1]*School of Physics and Wuhan National Laboratory for Optoelectronics, Huazhong University of Science and Technology, Wuhan 430074, China*

[2]*Laboratory of Optical Information Technology, Wuhan Institute of Technology, Wuhan 430205, China*

(Received 9 March 2016; revised manuscript received 3 May 2016; published 25 July 2016)

We theoretically investigate the electron interference dynamics of H_2^+ in an intense infrared laser field. At intermediate internuclear distances, an interference fringe appears in the electron momentum distribution. By tracing the time evolution of the electron density, we identify an internal scattering channel of the electrons. The observed fringe is attributed to the interference between the internal scattered and direct photoelectrons. Our results reveal that the electron behaviors inside a molecule can be mapped onto the experimentally accessible photoelectron momentum spectra, suggesting a time-resolved way of probing the complex laser-driven electron dynamics on an attosecond time scale.

DOI: 10.1103/PhysRevA.94.013422

I. INTRODUCTION

Laser-induced tunneling ionization of atoms and molecules is one of the most fundamental processes in attosecond physics, and it is the starting point for a range of strong-field phenomena, including high-order harmonics and attosecond pulse generation [1–3], above-threshold ionization [4–7], laser-induced electron diffraction [8,9], and nonsequential double ionization [10–12]. For atoms, the tunneling process is well understood by the quasistatic tunneling ionization picture [13,14], especially in the long-wavelength and strong-intensity regime characterized by the Keldysh parameter [15] $\gamma < 1$ ($\gamma = \omega\sqrt{2I_p}/E_0$ where ω and E_0 are the laser field frequency and amplitude, respectively, and I_p is the atomic ionization potential). For molecules, even the simplest H_2^+, the underlying ionization process becomes more complicated. It has been demonstrated that when the H_2^+ molecule is stretched to intermediate internuclear distances, typically in the range of 5–12 a.u. (atomic units are used), the ionization rate sharply increases, exceeding the rate of the separated-atom limit by one order of magnitude. This phenomenon is called charge-resonance enhanced ionization (CREI) [16–19] and it has already been experimentally observed [20–22]. Besides the CREI, it has been shown that there are multiple ionization bursts (MIBs) within one-half cycle of the laser field due to the transient localization of the electrons at one of the protons [23–26]. The subcycle oscillation occurs on an attosecond time scale, indicating an even more complex laser-driven electron dynamics during tunneling. Thus, methods to probe the complex electron dynamics inside the molecule are highly demanding.

Photoelectron spectroscopy based on electron wave packet interferences has shown its ability and great advantages in investigating attosecond dynamics. Strong-field photoelectron holography (SFPH) is one of the fascinating applications for its potential to probe structural information of the targets as well as the involved laser-driven process [27–31]. The SFPH pattern was first observed in photoelectron momentum distribution (PMD) of metastable xenon using a midinfrared 7 μm laser pulse [27] and then extended to other atoms and molecules [29]. It manifests itself as a forklike interference structure in the PMD. Theoretical analysis has shown that SFPH originates from the interference between electrons directly flowing to the detector (reference wave) after tunneling and those undergoing near-forward scattering (signal wave) by the parent core. Here in this work, we show that for H_2^+ at intermediate internuclear distances, i.e., in the CREI region, electrons released from the upper hill are forward scattered by the other core, forming an internal scattering channel. The scattering electrons interfere with the direct electrons, which can be identified as another kind of SFPH. The internal scattering process is confined within the time scale of a small fraction of the laser optical cycle, usually a few hundred attoseconds. Thus, this kind of hologram in the PMD encodes the attosecond electron dynamics and is capable of probing the ultrafast dynamics in the strong-field ionization of molecules.

II. RESULTS AND DISCUSSION

To this end, we numerically solve the time-dependent Schrödinger equation (TDSE) for the two-dimensional (2D) model of H_2^+ with different fixed internuclear distances R. Previous calculations have shown that the coupling between the electronic and nuclear motions does not influence the CREI significantly [23,32]; thus the fixed nuclear assumption is valid in our case. A soft-core potential is adopted with a screening parameter closely reproducing the ionization energies of the two lowest lying $1s\sigma_g$ and $2p\sigma_u$ states. The laser intensity is 2×10^{14} W/cm^2 with a wavelength of 800 nm. The vector potential is given by $\mathbf{A}(t) = E_0/\omega \cos^2(\pi t/\tau)\sin(\omega t)\mathbf{e}_x$ with the total duration $\tau = 5T$ (T is the optical cycle). The corresponding electric field is $\mathbf{E}(t) = -\partial\mathbf{A}(t)/\partial t$. The wave function is propagated using the Fourier-grid Hamiltonian split-operator method [33]. After the end of the laser pulse, the wave function is further propagated for an additional four optical cycles to ensure all the ionized components move away from the core. The PMD is calculated by a Fourier transform of the ionized wave function. The latter is obtained using a $\cos^{1/2}$-mask function to filter out the bound part of the wave function.

*zhouymhust@hust.edu.cn
†lupeixiang@hust.edu.cn

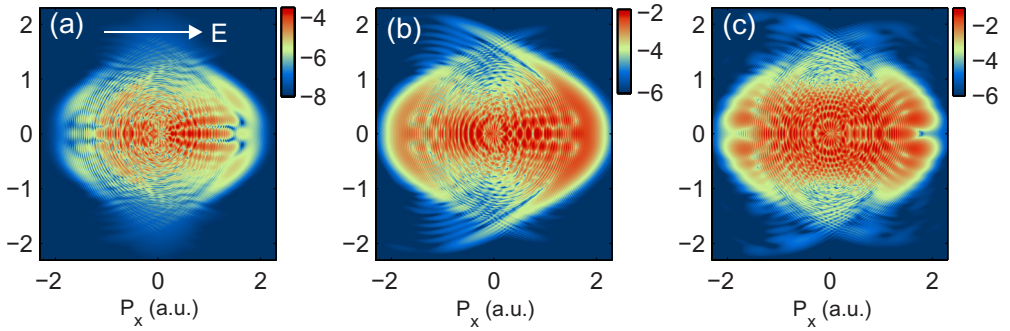

FIG. 1. Photoelectron momentum distributions of H_2^+ calculated from the 2D TDSE for different internuclear distances (a) $R = 2$, (b) $R = 4$, and (c) $R = 8$ a.u. The color coding is on a logarithmic scale. The laser intensity is 2×10^{14} W/cm^2 and the wavelength is 800 nm. The laser polarization direction is along the x axis in parallel with the molecular axis, as indicated by the right arrow in (a).

Figure 1 shows the PMDs for internuclear distances $R = 2$, 4, and 8, respectively. The laser is polarized in parallel with the molecular axis. As displayed in Fig. 1(a), for $R = 2$ a.u., a clear forklike structure appears, which is the previously observed near-forward scattering photoelectron hologram [27]. It originates from the interference of electrons released at the same quarter cycle of the laser pulse, following two paths en route to the detector. In one path the electron moves directly to the detector with negligible interaction with the molecular ions. In the other path, before reaching the detector, the electron is driven back and near-forward rescattered off by the parent ion [27]. As the molecule is stretched to $R = 4$ a.u., the forklike holographic pattern is still visible, shown in Fig. 1(b). When the molecule is further stretched to 8 a.u. in Fig. 1(c), i.e., in the CREI region, a semiring structure with an incoming form (i.e., with an rightward curvature) dominates in the PMD. As can be seen from the right side of the PMD where $p_x > 0$, the main feature of this interference pattern is that the width of the interference stripes as well as the space between adjacent stripes becomes larger with the increase of p_x. The forklike structure is still visible but becomes less conspicuous.

In order to explore the physical mechanisms leading to these semiring interference structures, we trace the time evolution of the electron density along the laser polarization direction (x direction). This is done by recording the electron wave function and then integrating it over the transverse direction at each time step during the time propagation. In this way the dynamical evolution of the electron density of the molecular system as a function of time can be visualized, as presented in Fig. 2(a). There are three main features that can be observed. First, the ionization mainly occurs near the peak of the laser field around two instants $t = 2T$ and $t = 2.5T$. We define the molecular core located at $R = -4$ a.u. as the left core and the other one located at $R = 4$ a.u. as the right core. At $t = 2T$ the electric field is positive such that the right core is up-hill and at $t = 2.5T$ the electric field is negative and thus the left core is up-hill. The electron density evolution indicates that the electron localized at the up-hill can directly tunnel through the internal potential core and form the dominant ionization channel at $R = 8$ a.u., in agreement with the intuitive physical picture of CREI [17]. Second, there are not only one but multiple ionization bursts within a half cycle of the laser field, marked as A, B, A', and B' in Fig. 2(a). Previous studies have shown that the MIBs result from transient electron localization at one of the molecular cores on the attosecond time scale [23,26]. The underlying mechanisms can be elucidated using a simple two-state model incorporating the quasidegenerate lowest lying states of H_2^+, i.e., the ground $1s\sigma_g$ ($|g\rangle$) and the first-excited $2p\sigma_u$ ($|u\rangle$) states. The localized electron wave function at each proton can be expressed as $|L\rangle = (|g\rangle - |u\rangle)/\sqrt{2}$ and $|R\rangle = (|g\rangle + |u\rangle)/\sqrt{2}$ [34,35]. The global phases of $|g\rangle$ and $|u\rangle$ are chosen such that $|L\rangle$ and $|R\rangle$ represent electrons localized at the left and right cores, respectively. We calculate the evolution of localized electron populations $P_L(t) = \langle L|\Psi(t)\rangle^2$ and $P_R(t) = \langle R|\Psi(t)\rangle^2$ at the two protons, shown in Fig. 2(b). The oscillations of localized populations indicate the transient coupling between the two protons; thus the electrons are driven between the two protons

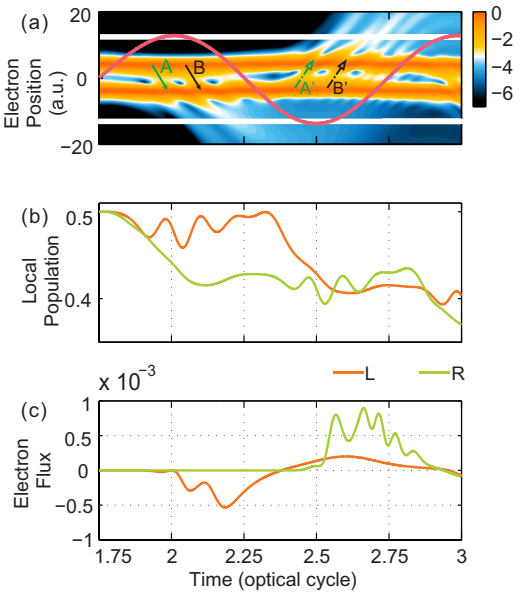

FIG. 2. (a) Electron density integrated over the y direction as a function of time and coordinate x at $R = 8$ a.u., plotted on a logarithmic scale. The red solid curve is the laser field. (b) Electron population localized at the left (orange solid curve) and right (green solid curve) cores, respectively. (c) Electron probability flux at left $x_L = -R/2 - 10$ (orange solid curve) and right $x_R = R/2 + 10$ (green solid curve). We define right as the positive direction.

during the interaction with the laser field. Two sharp decreases of the population can be observed: one is $P_R(t)$ around $t = 2T$ and the other is $P_L(t)$ near $t = 2.5T$, corresponding to two dominant events of MIBs.

Both results indicate complex electron dynamics inside the molecule under the influence of the laser field, where there is no observable to prove it. Fortunately, a third feature can be found in Fig. 2(a). Electrons that tunnel from the first half cycles can turn around and pass through the plane of the parent ion when the electric field reverses its sign at the adjacent half cycle. However, these electrons are not scattered by the ion due to the transverse momentum at tunneling and are referred to as direct electrons. This part of the electron wave packet interferes with the electron wave packet released at the second half cycle, showing the clear fine interference fringes at the region $|x| \geqslant 10$ a.u., as can be seen in Fig. 2(a). We also calculate the electron probability flux at the boundaries $x_L = -R/2 - 10$ (orange solid curve) and $x_R = R/2 + 10$ (green solid curve), shown in Fig. 2(c). The electron first moves out the left boundary around $t = 2.25T$. Oscillation of the probability flux is the evidence of MIBs. Then within $2.5T$–$2.75T$, part of the electrons can be driven back and across the left boundary from the opposite side, forming wide lobes in the flux. The reversed electrons further move to the right boundary and interfere with electrons released near $t = 2.5T$. The fine interference fringe near the right boundary manifests itself as the semiring structure in the PMD in Fig. 1(c).

Next we analyze the alignment dependence of the PMDs. Figure 3 presents the PMDs in the laboratory frame at internuclear distance $R = 8$ a.u. with alignment angles of 0°, 30°, 60°, and 90°, respectively. In Fig. 3(a), the laser polarization is parallel to the molecular axis. The semiring pattern with right curvature in the positive momentum region is clearly observed. When the alignment angles are increased to 30° and 60°, the momentum distributions are distorted as presented in Figs. 3(b) and 3(c). The semiring interference pattern shown in Fig. 3(a) cannot be well resolved any more. As the alignment angle is further increased to 90° in Fig. 3(d), only the forklike pattern, i.e., the forward scattering hologram, can be observed and the semiring pattern has totally disappeared. This phenomenon can be attributed to the fact that with the increasing of the orientation angle, the two cores are not parallel to the laser polarization; thus electrons that tunnel from the up-hill core will miss the down-hill core and the internal scattering channel is switched off. As a result, the semiring pattern originating from the interference between direct and internal scattering channels has disappeared for the perpendicular orientation. Besides, the PMD shown in Fig. 3(d) exhibits side lobes in the orthogonal direction which are different from that of the atomic case. A possible explanation for the side lobes could be related to the two-center interference effect [36]. The two-center interference features stem from the emission of electrons from different molecular cores, leading to interference in a similar way as in a double-slit experiment. The orientation dependence of the momentum distributions provides strong evidence that the electron propagation and scattering process inside the molecule are responsible for the semiring structure.

Using an alternative presentation, we take a snapshot of the 2D electron probability density in coordinate space from the numerical results in Fig. 4(a) at the instant of $t = 2.7T$ where the direct and internal scattering parts of

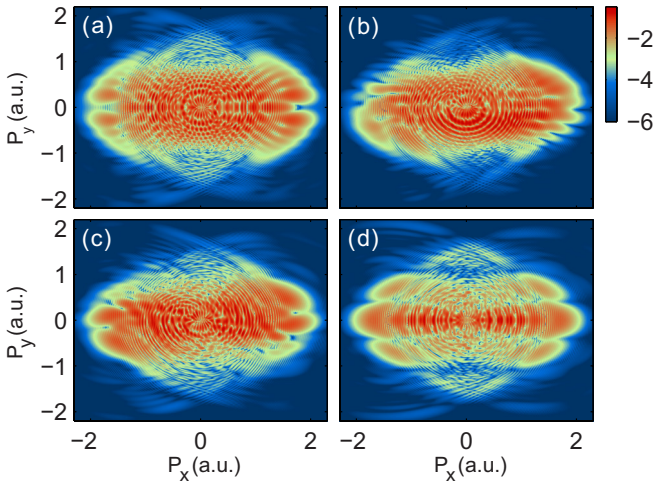

FIG. 3. Photoelectron momentum distributions of H_2^+ calculated from the 2D TDSE for different alignment angles (a) 0°, (b) 30°, (c) 60°, and (d) 90° at internuclear distance $R = 8$ a.u. in the laboratory frame. The color coding is on a logarithmic scale. Laser parameters are the same as in Fig. 1.

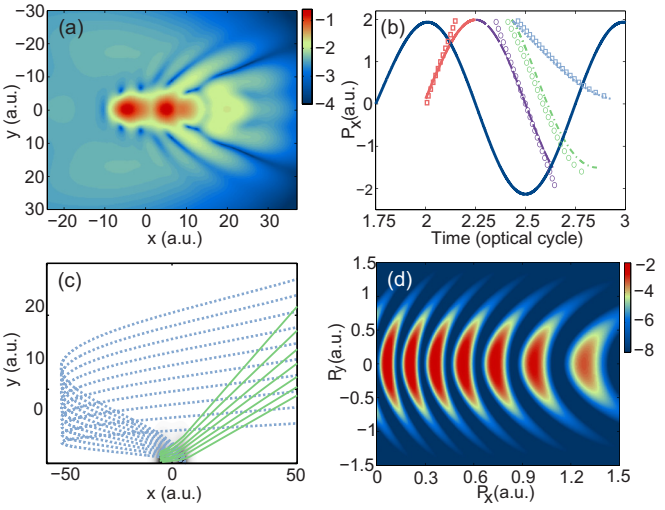

FIG. 4. (a) Snapshot of the two-dimensional electron distribution in coordinate space at $t = 2.7T$. The color coding is on a logarithmic scale. (b) Classical and SFA predictions of ionization and rescattering (revisiting) times for internal scattering (direct) electrons. The electric field is shown by the dark blue solid line. Ionization (red solid line) and revisiting (light blue dotted line) times for direct electrons and ionization (purple dashed line) and rescattering (light green dashed-dotted line) times for internal scattering electrons are extracted from the classical model. The corresponding SFA predictions are shown by squares and circles, respectively. (c) Sample electron trajectories for direct (light blue dotted lines) and internal scattering (light green solid lines) paths. (d) Interference pattern between direct and internal scattering channels predicted by the SFA model, plotted on a logarithmic scale.

the electron wave packet overlap. The snapshot captures the essential interference event between direct and internal scattering electrons. Several interference stripes are clearly seen in Fig. 4(a). In what follows, we adopt the molecular strong field approximation (MO-SFA) model [37–41] to show how the ionization timing information is encoded in the PMD. Here, we use the length-gauge version of the MO-SFA with the initial state dressed by the laser field. Previous studies have shown that the "dressed state" MO-SFA in length gauge gives best agreement with the experimental data and TDSE results for diatomic molecules with large internuclear distances [42,43]. In analogy to the previous SFPH, we refer to the direct electrons as the reference wave and the internal scattering wave as the signal wave. The semiclassical actions of the two parts are expressed as

$$S_{\rm ref} = \frac{1}{2}\int_{t_i^{\rm ref}}^{t} d\tau[\mathbf{p}+\mathbf{A}(\tau)]^2 - I_p t_i^{\rm ref} \tag{1}$$

and

$$\begin{aligned} S_{\rm sig} = {} & \frac{1}{2}\int_{t_i^{\rm sig}}^{t_r^{\rm sig}} d\tau[\mathbf{k}+\mathbf{A}(\tau)]^2 - I_p t_i^{\rm sig} \\ & -\mathbf{k}\cdot\mathbf{R} + \left[\mathbf{A}\left(t_i^{\rm sig}\right) - \mathbf{A}\left(t_r^{\rm sig}\right)\right]\cdot\mathbf{R}/2 \\ & +\frac{1}{2}\int_{t_r^{\rm sig}}^{t} d\tau[\mathbf{p}+\mathbf{A}(\tau)]^2, \end{aligned} \tag{2}$$

where $t_i^{\rm ref}$ and $t_i^{\rm sig}$ are the complex ionization times of the reference and signal waves, respectively, and $t_r^{\rm sig}$ is the scattering time of the signal wave, which can be found by the saddle point method. $\mathbf{p}=(p_x,p_y)$ is the final momentum and $\mathbf{k}=(k_x,k_y)$ is the canonical momentum before scattering. I_p is the ionization potential of the molecule. The original SFA theory [44] assumes that the electron leaves and returns to the geometric center of the molecule. This is reasonable for molecules with small internuclear distances. For relatively large internuclear distances, electron trajectories along with electrons whose travels start at one ion and end at the other should be taken into account. This displacement leads to the third and fourth additional terms on the right-hand side of Eq. (2), in comparison with the original formulation.

For electrons that leave from the left core and then scatter with the right one, the condition for saddle momentum $\mathbf{k}$ is $\nabla_{\mathbf{k}} S_{\rm sig}(\mathbf{k},\mathbf{p},t_i^{\rm sig},t_r^{\rm sig})|_{\mathbf{k}=\mathbf{k_s}} = \mathbf{R}$, which gives $\mathbf{k_s} = \int_{t_i^{\rm sig}}^{t_r^{\rm sig}} dt'\mathbf{A}(t')/(t_r^{\rm sig}-t_i^{\rm sig}) + \mathbf{R}/(t_r^{\rm sig}-t_i^{\rm sig})$. Together with the other two saddle equations regarding ionization and rescattering times $t_i^{\rm sig}$ and $t_r^{\rm sig}$, the saddle point $(\mathbf{k_s},t_i^{\rm sig},t_r^{\rm sig})$ can be found for each final momentum $\mathbf{p}$. Here, we choose saddle point solutions that electrons leave the left core and propagate directly to the right core, i.e., the internal scattering electron trajectories. The real part of the ionization (purple circles) and rescattering (green circles) times as a function of final momentum (along the polarization axis) is shown in Fig. 4(b). The real part of the ionization (red squares) and revisiting (blue squares) times (without scattering) for direct electrons are also shown. Sample electron trajectories for reference (blue dotted lines) and signal (green solid lines) waves are shown in Fig. 4(c). One can see that the reference wave first tunnels from the right core after $t=2T$ and propagates to the left, then reverses its direction as the sign of the electric field is changed. The signal wave tunnels from the left core near $t=2.5T$ and moves to the right. Near $t=2.7T$, it is scattered by the right core and then propagate to the detector. The final momentum spectrum is evaluated by $|\sum \exp[-iS_{\rm ref}(t_{is}^{\rm ref})] + \sum \exp[-iS_{\rm sig}(t_{is}^{\rm sig},t_{rs}^{\rm sig})]|^2$ where the preexponential terms are omitted for simplicity. The results are presented in Fig. 4(d). One can see that the overall shapes of the internal scattering hologram are clearly revealed without preexponential terms.

By analyzing the phase difference between the reference and signal waves, we will show how the attosecond time-resolved electron dynamics inside the molecules has been recorded in this kind of interference. Using Eqs. (1) and (2), The phase difference is given by

$$\begin{aligned} \Delta S = {} & S_{\rm sig} - S_{\rm ref} \\ = {} & -\frac{1}{2}p_y^2\left[{\rm Re}\left(t_r^{\rm sig}\right) - {\rm Re}(t_i^{\rm ref})\right] \\ & -\frac{1}{2}\int_{{\rm Re}(t_i^{\rm sig})}^{{\rm Re}(t_r^{\rm sig})} d\tau[{\rm Re}(k_x)+A(\tau)]^2 \\ & +\frac{1}{2}\int_{{\rm Re}(t_i^{\rm ref})}^{{\rm Re}(t_r^{\rm sig})} d\tau[p_x+A(\tau)]^2 + I_p\left[{\rm Re}\left(t_i^{\rm sig}\right) - {\rm Re}\left(t_i^{\rm ref}\right)\right] \\ & -{\rm Re}(k_x)R + {\rm Re}\left[A\left(t_i^{\rm sig}\right) - A\left(t_r^{\rm sig}\right)\right]R/2 + \Delta S^{Im}. \end{aligned} \tag{3}$$

Here, we split the semiclassical action into real and imaginary parts by using the real part of the complex saddles; thus the first six terms become real. ΔS^{Im} is the imaginary part representing the difference of semiclassical action during the under-barrier motion of the electrons. We present real classical ionization and rescattering (revisiting) times in Fig. 4(b) by setting $I_p=0$ and find that they are very close to the SFA predictions. Thus the last term has little influence on the interference structure. The first term on the right-hand side represents the phase difference in the orthogonal direction. The second and third terms are the phase differences in the parallel direction. The forth term is caused by the difference in ionization times for reference and signal waves. The fifth and sixth terms are phases of the signal wave acquired in the internal motion, which are related to the structure parameter R. For the previously observed near-forward scattering holography [27], only the first term dominates the formation of the hologram. For the present case, the reference and signal electrons librate from different half cycles, and thus the second and third terms also contribute to the total difference. From these two terms, one can find that both $t_i^{\rm sig}$ and $t_r^{\rm sig}$ depend on p_x; thus interference stripes appear in the longitudinal direction. Besides, the fifth and sixth terms indicate that the interference also depends on the internuclear distance, i.e., the structure information of the target. In order to further illustrate this point, we present the comparison of PMDs in Fig. 5 for internuclear distances $R=8$ and 10 a.u. One can clearly see the change of semiring interference fringes at different internuclear distances, both the shape and the spacing between them, proving that the structure information is encoded in the internal-scattering hologram, in accordance with our SFA analysis.

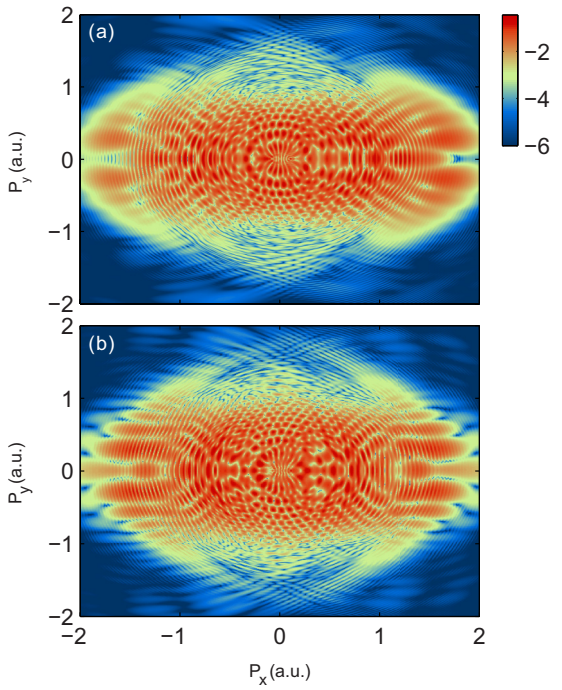

FIG. 5. Photoelectron momentum distributions of H_2^+ calculated from the 2D TDSE for different internuclear distances (a) $R = 8$, and (b) $R = 10$ a.u. The color coding is on a logarithmic scale. Laser parameters are the same as in Fig. 1.

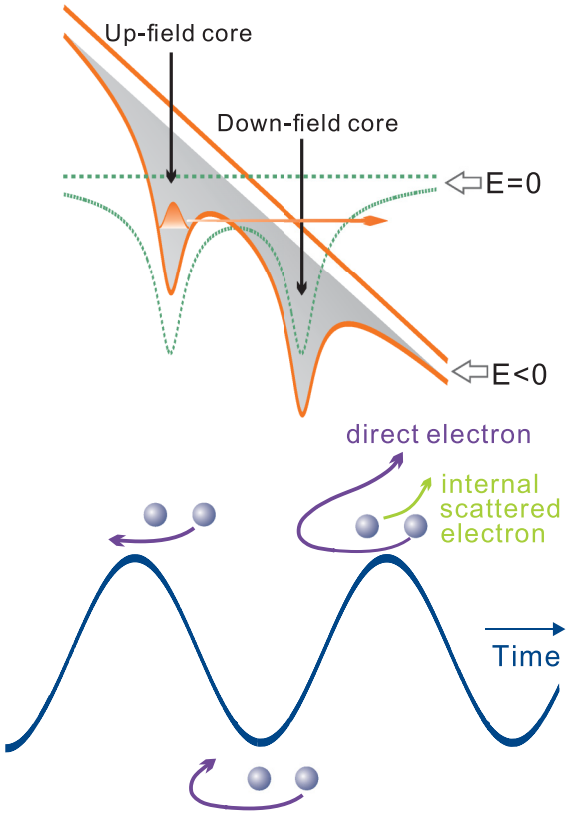

FIG. 6. Sketch of interference between direct and internal scattering electrons.

III. CONCLUSION

In conclusion, at intermediate internuclear distance of the H_2^+ molecule where the CREI mechanism is dominating for electron ionization, the PMD presents a set of incoming semirings. By tracing the time evolution of the electron probability density, we introduce an intuitive picture for the origin of the interference structures, as summarized in Fig. 6. First, the Coulomb potential of the molecule is distorted by the laser field. Electrons localized at the up-field core tunnel through the stretched inner Coulomb potential towards the down-field core and then are scattered off, which is viewed as an internal scattering channel. The scattering electrons interfere with direct electrons librated at earlier times, forming the semiring interference stripes in PMD. This holographic interference pattern has recorded temporal information of electron behaviors inside the molecule with subcycle time resolution, suggesting that it is possible to probe complex laser-driven inner electron dynamics using the experimentally accessible PMD.

ACKNOWLEDGMENTS

We thank Dr. Xue-Bin Bian for helpful discussions. This work was supported by the National Natural Science Foundation of China under Grants No. 61405064, No. 11234004, and No. 61475055. Numerical simulations presented in this paper were carried out using the High Performance Computing Center experimental testbed in SCTS/CGCL.

[1] F. Krausz and M. Ivanov, Rev. Mod. Phys. **81**, 163 (2009).
[2] Y. Mairesse, A. de Bohan, L. J. Frasinski, H. Merdji, L. C. Dinu, P. Monchicourt, P. Breger, M. Kovaěev, R. Taïeb, B. Carré, H. G. Muller, P. Agostini, and P. Salières, Science **302**, 1540 (2003).
[3] L. He, P. Lan, Q. Zhang, C. Zhai, F. Wang, W. Shi, and P. Lu, Phys. Rev. A **92**, 043403 (2015); C. Zhai *et al.*, Sci. Rep. **6**, 23236 (2016); X. Zhu, X. Liu, Y. Li, M. Qin, Q. Zhang, P. Lan, and P. Lu, Phys. Rev. A **91**, 043418 (2015); X. Zhu *et al.*, Opt. Express **20**, 16275 (2012).
[4] D. B. Milošević and F. Ehlotzky, Adv. At. Mol. Opt. Phys. **49**, 373 (2003).
[5] D. B. Milošević, G. G. Paulus, D. Bauer, and W. Becker, J. Phys. B: At. Mol. Opt. Phys. **39**, R203 (2006).
[6] M. Li, P. Zhang, S. Luo, Y. Zhou, Q. Zhang, P. Lan, and P. Lu, Phys. Rev. A **92**, 063404 (2015).
[7] Y. Li, P. Lan, H. Xie, M. He, X. Zhu, Q. Zhang, and P. Lu, Opt. Express **23**, 28801 (2015); X. Zhu, P. Lan, K. Liu, Y. Li, X. Liu, Q. Zhang, I. Barth, and P. Lu, *ibid.* **24**, 4196 (2016).
[8] M. Meckel, D. Comtois, D. Zeidler, A. Staudte, D. Pavičić, H. C. Bandulet, H. Pépin, J. C. Kieffer, R. Dörner, D. M. Villeneuve, and P. B. Corkum, Science **320**, 1478 (2008).

[9] C. Blaga, J. Xu, A. D. DiChiara, E. Sistrunk, K. Zhang, P. Agostini, T. A. Miller, L. F. DiMauro, and C. D. Lin, Nature (London) **483**, 194 (2012).
[10] Th. Weber, H. Giessen, M. Weckenbrock, G. Urbasch, A. Staudte, L. Spielberger, O. Jagutzki, V. Mergel, M. Vollmer, and R. Dörner, Nature (London) **405**, 658 (2000).
[11] W. Becker, X. Liu, P. J. Ho, and J. H. Eberly, Rev. Mod. Phys. **84**, 1011 (2012).
[12] A. Tong, Y. Zhou, and P. Lu, Opt. Express **23**, 15774 (2015); X. Ma, Y. Zhou, and P. Lu, Phys. Rev. A **93**, 013425 (2016).
[13] A. M. Perelomov, V. S. Popov, and M. V. Terentev, Sov. Phys. JETP **23**, 924 (1966).
[14] M. V. Ammosov, N. B. Delone, and V. P. Kralnov, Sov. Phys. JETP **64**, 1191 (1986).
[15] L. V. Keldysh, Sov. Phys. JETP **20**, 1307 (1965).
[16] T. Seideman, M. Y. Ivanov, and P. B. Corkum, Phys. Rev. Lett. **75**, 2819 (1995).
[17] T. Zuo and A. D. Bandrauk, Phys. Rev. A **52**, R2511 (1995).
[18] C. Huang, P. Lan, Y. Zhou, Q. Zhang, K. Liu, and P. Lu, Phys. Rev. A **90**, 043420 (2014).
[19] G. L. Kamta and A. D. Bandrauk, Phys. Rev. Lett. **94**, 203003 (2005).
[20] E. Constant, H. Stapelfeldt, and P. B. Corkum, Phys. Rev. Lett. **76**, 4140 (1996).
[21] J. Wu, M. Meckel, L. Ph. H. Schmidt, M. Kunitski, S. Voss, H. Sann, H. Kim, T. Jahnke, A. Czasch, and R. Dörner, Nat. Commun. **3**, 1113 (2012).
[22] H. Xu, F. He, D. Kielpinski, R. T. Sang, and I. V. Litvinyuk, Sci. Rep. **5**, 13527 (2015).
[23] N. Takemoto and A. Becker, Phys. Rev. Lett. **105**, 203004 (2010).
[24] N. Takemoto and A. Becker, J. Chem. Phys. **134**, 074309 (2011).
[25] F. He, A. Becker, and U. Thumm, Phys. Rev. Lett. **101**, 213002 (2008).
[26] N. Takemoto and A. Becker, Phys. Rev. A **84**, 023401 (2011).
[27] Y. Huismans, A. Rouzée, A. Gijsbertsen, J. Jungmann, A. Smolkowska, P. Logman, F. Lépine, C. Cauchy, S. Zamith, T. Marchenko, J. Bakker, G. Berden, B. Redlich, A. van der Meer, H. Muller, W. Vermin, K. Schafer, M. Spanner, M. Ivanov, O. Smirnova, D. Bauer, S. Popruzhenko, and M. Vrakking, Science **331**, 61 (2011).
[28] Y. Huismans, A. Gijsbertsen, A. S. Smolkowska, J. H. Jungmann, A. Rouzée, P. S. W. M. Logman, F. Lépine, C. Cauchy, S. Zamith, T. Marchenko, J. M. Bakker, G. Berden, B. Redlich, A. F. G. van der Meer, M. Yu. Ivanov, T.-M. Yan, D. Bauer, O. Smirnova, and M. J. J. Vrakking, Phys. Rev. Lett. **109**, 013002 (2012).
[29] M. Meckel, A. Staudte, S. Patchkovskii, D. M. Villeneuve, P. B. Corkum, R. Dörner, and M. Spanner, Nat. Phys. **10**, 594 (2014).
[30] Y. Zhou, O. I. Tolstikhin, and T. Morishita, Phys. Rev. Lett. **116**, 173001 (2016); X. B. Bian and A. D. Bandrauk, *ibid.* **108**, 263003 (2012).
[31] X. B. Bian, Y. Huismans, O. Smirnova, K. J. Yuan, M. J. J. Vrakking, and A. D. Bandrauk, Phys. Rev. A **84**, 043420 (2011); M. He, Y. Li, Y. Zhou, M. Li, and P. Lu, *ibid.* **93**, 033406 (2016).
[32] M. Odenweller, N. Takemoto, A. Vredenborg, K. Cole, K. Pahl, J. Titze, L. Ph. H. Schmidt, T. Jahnke, R. Dörner, and A. Becker, Phys. Rev. Lett. **107**, 143004 (2011).
[33] M. D. Feit, J. A. Fleck, Jr., and A. Steiger, J. Comput. Phys. **47**, 412 (1982).
[34] R. S. Mulliken, J. Chem. Phys. **7**, 20 (1939).
[35] K. C. Kulander, F. H. Mies, and K. J. Schafer, Phys. Rev. A **53**, 2562 (1996).
[36] J. Henkel, M. Lein, and V. Engel, Phys. Rev. A **83**, 051401(R) (2011).
[37] O. Smirnova, M. Spanner, and M. Ivanov, J. Mod. Opt. **54**, 1019 (2007).
[38] C. C. Chirilă and M. Lein, Phys. Rev. A **73**, 023410 (2006).
[39] C. C. Chirilă and M. Lein, Phys. Rev. A **74**, 051401(R) (2006).
[40] D. B. Milošević, Phys. Rev. A **74**, 063404 (2006).
[41] M. Busuladžić, A. Gazibegović-Busuladžić, D. B. Milošević, and W. Becker, Phys. Rev. Lett. **100**, 203003 (2008).
[42] W. Becker, J. Chen, S. G. Chen, and D. B. Milošević, Phys. Rev. A **76**, 033403 (2007).
[43] M. Busuladžić and D. B. Milošević, Phys. Rev. A **82**, 015401 (2010).
[44] M. Lewenstein, Ph. Balcou, M. Yu. Ivanov, A. L'Huillier, and P. B. Corkum, Phys. Rev. A **49**, 2117 (1994).